

# Materials Research Express



## PAPER

# Investigations on micro hardness, electrical and thermal conductivity of AA7075 surface hybrid composites produced through friction stir processing

RECEIVED  
9 May 2019

REVISED  
14 September 2019

ACCEPTED FOR PUBLICATION  
25 September 2019

PUBLISHED  
4 October 2019

K Suganeswaran<sup>1,4</sup> , R Parameshwaran<sup>1</sup>, P Thangavel<sup>2</sup>, N Nithyavathy<sup>1</sup> and T Sivasakthivel<sup>3</sup>

<sup>1</sup> Department of Mechatronics Engineering, Kongu Engineering College, Perundurai, Erode, 638060, India

<sup>2</sup> Department of Mechanical Engineering, Kongu Engineering College, Perundurai, Erode, 638060, India

<sup>3</sup> Department of Mechanical Engineering and Vehicle Technology, Global College of Engineering and Technology (GCET), University of west of England, Bristol, Oman

<sup>4</sup> Author to whom any correspondence should be addressed.

E-mail: [suganeswaran22@gmail.com](mailto:suganeswaran22@gmail.com), [parameshwaran76@gmail.com](mailto:parameshwaran76@gmail.com), [ptvelmech@gmail.com](mailto:ptvelmech@gmail.com), [nithyavathy11@gmail.com](mailto:nithyavathy11@gmail.com) and [sivasakthivel.t@gmail.com](mailto:sivasakthivel.t@gmail.com)

**Keywords:** friction stir processing, composites, thermal conductivity, electrical conductivity, micro-hardness, coefficient of thermal expansion, ceramics

## Abstract

High strength, minimum thermal and electrical conductivity are the major requirements of aircraft applications which could be obtained by micro-structural modifications of the composites with particulate reinforcements. The proposed work focus the analysis on the behavior of micro hardness, coefficient of thermal expansion, thermal and electrical conductivity of AA7075 fabricated by friction stir processing with different weight ratios of Al<sub>2</sub>O<sub>3</sub> and SiC. Different surface hybrid composites are formed by varying the weight ratios. It ensures the formation of fine grained structure and decrease in thermal and electrical conductivity values with addition of higher hardness. During the friction stir processing, the working temperature is identified between 99.4 and 316.6 °C for the proposed composites, which shows 15.6% and 49.8% that of the melting point of AA7075 (635 °C). Experimental investigation on thermal conductivity and electrical conductivity has been conducted under different heat input values through varying the applied voltage from 25 to 225 V. The observation shows surface hybrid composites depicts lower conductivity values with Al<sub>2</sub>O<sub>3</sub> and SiC particles due to variation in energy level of electrons and phonons. Among the observations, the specimen S<sub>5</sub> reinforced with equal weight ratios of Al<sub>2</sub>O<sub>3</sub> and SiC yields the maximum micro-hardness of about 265 VHN and lower coefficient of thermal expansion of about 13 μm m<sup>-1</sup> °C. This is due to the reinforcement behavior and formation of Al<sub>4</sub>C<sub>3</sub> intermetallics. The morphological analysis also supports the requirements of aircraft components.

## Nomenclature

FSP	Friction stir processing
AMMC's	Aluminium Metal Matrix Composites
SHC's	Surface Hybrid Composites
CTE	Coefficient of Thermal Expansion
MMC's	Metal Matrix Composites
SEM	Scanning Electron Microscopy
XRD	X-ray Diffraction
IACS	International Annealed Copper Standard
TMA	Thermo-mechanical Analyzer

VHN	Vickers Hardness Value
BSE	Backscattered-Electron
FESEM	Field Emission Scanning Electron Microscope
$L_0$	Lorentz Number
$\sigma$	Electrical Conductivity
T	Temperature
Q	Heat Transfer Rate
k	Thermal Conductivity
A	Cross section Area of the Specimen
dT	Difference between the Surface Temperature
dx	Thickness of the Specimen
$k_p$	Phononic Heat Conductivity
$k_e$	Electronic Heat Conductivity

## 1. Introduction

Salient features like light weight, wear resistance, stiffness, specific strength, creep, fatigue nature, attractive thermal, and electrical characteristics has made Aluminium Metal Matrix Composites (AMMC's) as a major focus in aerospace industries. Various liquid-state processing methods like stir casting, compo casting, squeeze casting and infiltration methods are available for production of AMMC's. These methods are having the shortfalls like detrimental phase formation, shrinkage, porosity and inclusions that could be overcome by the solid state processing techniques. Among the numerous solid state processes, FSP is a convenient surface modification technique used to refine the microstructure of base metal [1]. The frictional effect between the rotating tool and base material induces heat that propagates softening and plasticization of the counterpart [2–4]. During this operation, the processed material is forged to back of the pin from the front end. This material transformation along with vigorous stirring action of the tool results in fine and equi-axed micro-structural grains [5, 6]. The defects like porosity, particle clustering, and agglomerations formed in the casting are also decreased during FSP [7].

The heat induced in FSP plays a vital role in controlling the microstructure and mechanical properties of base matrix [8, 9]. The accumulation of heat generated at tool shoulder, pin tip and side surface contributes to the total heat generation during FSP [10, 11]. This leads to the plastic deformation and also contributes some additional heat, but at a reduced amount than the frictional heat between the tool shoulder and counterpart base material [12]. Amount of peak temperature and heat generation rate are significantly influenced by the FSP parameters such as rotational and transverse speeds, plunge depth, number of passes and tool tilt angle. Also, heat conduction rate depends on the thermal conductivity of the material and temperature gradient. Measurement of temperature is difficult in molten state metals during the processing stage and it is overcome by friction stir processed specimens which involves the solid state nature.

Increased hardness with substantial reduction of thermal and electrical conductivity is a major challenge faced in the manufacturing of aircraft components. To accomplish this feasibility, an attempt has been made on the fabrication of AA7075 using FSP with ceramic particle reinforcements. Wiedemann–Franz law ( $K = L_0 \sigma T$ ) describes the relation between both thermal and electrical conductivity, but the law breaks down between zero and Debye temperature [13]. In addition, Lee *et al* reported the law violation at cryogenic temperatures owing to the formation of unconventional phases and scattering of quasi particles. The effect of variation in temperature on thermal conductivity of metallic vanadium oxide under different conditions was carried out and reported that it does not obey the Wiedemann–Franz law due to transition of metal to insulator at higher temperatures [14]. Total thermal conductance is governed by Cartesian coordinate system and discussed about the heat transfer analysis at metallic quantum point contact level which indicates limited support of radiation level to heat transport [15].

Thermal conductivity of AA7075 is minimized by increasing the solute concentration in alloys that leads to scattering action of phonons and electrons at raised levels of temperature [16]. Curran *et al* conducted a study on measuring the thermal expansivity over oxide film coating in AA6082 and reported that the results are independent of coating thickness [17]. Thermal conductivity of alumina decreases with increase in temperature as a result of thermal shock resistance [18]. The mean free path of the free electrons is diverted by interaction between electrons-imperfections, electron- solute, and electron-electron interactions. Also, grain boundaries

and crystal defects enhances the scattering action of phonons and results in degradation of thermal conductivity [19].

Electrical resistivity increases due to thermal agitated atomic vibrations, vacancies, dislocations and the substitute of impurities in pure metal lattices [20]. The amount of porosity and impurity determines the electron scattering level which leads to variation in electrical resistivity [16]. Electrical conductivity of Aluminium alloy in solid solution is largely determined by the amount of alloying, volume and nature of precipitates [21, 22]. Also, the breakdown potential of the particular material varies widely during the addition of alloys which modifies the electrical conductivity behavior of the composites [23]. Cluster formations of magnesium and silicon in aluminium alloy causes distortion of lattice in addition to rise in hardness. This variation causes decrease in electrical conductivity [24]. Segregation of precipitates and porosity formed during resolidification process degrades the electrical conductivity at higher temperatures [25]. FSP treated surfaces possess better hardness value and further enhancement in hardness is obtained by incorporating ceramic particles as reinforcement. Increase in amount of  $B_4C$  particles on copper matrix increases the dislocation of base metal in turn raises the hardness value [26]. Hardness of AA7075-T6 is influenced through dispersion strengthening, individual hardness and pinning effect of  $B_4C$  particle on the grain boundary [27]. Strain mismatch between the SiC particles and AA1050 results in work hardening and intensify the dislocation density which confirms the increase in hardness value [8]. Amount of variation in phonon energy level are larger at higher range of hardness value [28]. Ni-B/SiC composite coatings are electrodeposited using trimethylamine borane as a precursor and attains enhancement in hardness with optimal SiC content. The agglomeration and formation of pores at higher SiC content paves way for declined hardness value. In order to increase the hardness, thermal treatment has been applied [29].

Several investigations have been attempted on thermal analysis about thermal conductivity and CTE of MMC's, but scanty amount was found related to SHC's processed using FSP. Karthikeyan *et al* reported that incorporation of SiC particles in AA7075 using stir casting technique reduces the heat capacity of the composites. Based on temperature, the heat capacity values does not follow a linear trend due to variation in atomic vibrations [30]. Compared to argon atmosphere, nitrogen gas is the key factor to hinder the formation of  $Al_4C_3$  intermetallics which provides the adhesion behaviour in between Al matrix and diamond reinforcements. During the experimentation, gas infiltration method had been applied and results show that reduction in interfacial thermal resistance between Al and diamond composites [31]. Thermal mismatch between the AA7075 and fly ash particles paves the way for increment in dislocations and holds the positive influence on the strength and CTE values. Negligible interaction between electrons and phonons was identified and proceeds to insignificant change in thermal conductivity [32]. Among the various available methods, electro deposition is the viable method for producing metal matrix composites (copper-diamond particle with TiC coating) for heat sink applications. This is attributed to the growth of copper matrix in an efficient way that closes the pores which play a vital role in thermal conductivity enhancement [33]. A theoretical numerical study was executed by Schindler *et. al* about the elastic and thermal properties of AA2024/SiC. For wide range of temperature (0–500)°C, the variation in thermal conductivity and thermal expansion is non-linear for this composite materials [34].

With reference to aircraft applications, higher hardness, lower coefficient of thermal expansion with minimum thermal and electrical conductivity is the essential characteristics. In order to meet the above requirements, significant micro structural modification with particle reinforcement is the prerequisite. So, the primary objective of this work is to elucidate the hardness, thermal and electrical behavior of AA7075 SHC's based on different combinations of  $Al_2O_3$  and SiC reinforcements processed using FSP which was not considered in previous literatures. The modified surface of alloy reinforced with different weight fraction of particles is called as SHC's. AA7075-T6 is opted owing to its higher specific strength and natural aging character along with hardenable precipitates.  $Al_2O_3$  and SiC are selected as reinforcements due to the reason of exceptional mechanical properties (Insulation character along with hardness) at elevated temperatures. Thermal and electrical conductivity of the composite specimens are measured by experimentally and analysis on morphological structure of the proposed combinations is executed. As per aircraft industrial need, the proposed SHC specimens could be employed as an alternate material for manufacturing aircraft components.

## 2. Materials and methodology

Work plate with the dimension (140 × 50 × 5) mm of AA 7075-T6 base material has been used in this experimental study.  $Al_2O_3$  -  $\alpha$  particle of 99.97% purity with an surface area of  $120 \text{ m}^2 \text{ g}^{-1}$  and SiC having purity of 99.8% and surface area of  $11 \text{ m}^2 \text{ g}^{-1}$  are used as reinforcements with an average size of 3  $\mu\text{m}$  and 2  $\mu\text{m}$  respectively. Reinforcement powders are purchased from Alfa aesar and the distinct weight ratios of  $Al_2O_3$  and

**Table 1.** Reinforcement details in specimens.

Specimen	Weight ratios of reinforcement	
	Al <sub>2</sub> O <sub>3</sub> (%)	SiC (%)
S <sub>1</sub>	Work plate (AA7075 Base Material)	
S <sub>2</sub>	Empty Pass or FSP without reinforcement	
S <sub>3</sub>	100	0
S <sub>4</sub>	75	25
S <sub>5</sub>	50	50
S <sub>6</sub>	25	75
S <sub>7</sub>	0	100

**Table 2.** Technical Specifications of FSP tool.

Measurement	Values
Shoulder diameter	25 mm
Pin diameter	6 mm
Pin length	3 mm
Rotational speed	1000 rpm
Travelling speed	56 mm min <sup>-1</sup>
Tilt angle with respect to vertical axis	2°
Pin Shape	Tapered cylindrical

SiC blends are identified based on the previous literature [35]. It is tightly packed in the groove of (2 × 2) mm made on the centre of work plate. The specimen numbers and their different compositions are shown in table 1.

FSP was executed on the specimens with pin less tool to seal the groove and followed by pinned tool with the selected parameters as mentioned in table 2.

Schematic representation of the FSP process along with the processed composite is shown in figures 1(a) and (b).

The micro-hardness, coefficient of thermal expansion, thermal and electrical conductivity values are experimentally determined for further analysis. Processing temperature measurement is carried out using a thermal imager (Make: Fluke) at a distance of 15 mm from the work specimen. The surface morphology of the specimens is analyzed through Optical microscopy (Make: METJI, JAPAN) and Scanning Electron Microscopy (JEOL, USA).

Structural analyses of the specimens are carried out using x-ray Diffraction (XRD, Xpert PRO) technique. Micro hardness values have been obtained for standard specimen of 5 mm width (cut in transverse section) along the FSP path using Vickers hardness indenter with a load of 50 N and a dwell period of 15 s. Indentations are made at a distance of 0.3 mm from the specimen surface. This procedure was repeated for three times on both processed and unprocessed specimens to obtain accurate results. Schematic along with experimental arrangement (Make: Sunstar Scientific) for the measurement of thermal and electrical conductivity are shown in figures 2 and 3 respectively. In order to know the voltage and current flow through the experimental system, digitalized ammeter and voltmeter are attached. The chamber is well insulated by glass wool in order to avoid the heat transfer interaction between the inside chamber and atmosphere. An auto transformer has been provided to vary the voltage from 25 to 230 V.

Specimens with the dimensions of (15 × 15 × 5) mm are considered for the conductivity analysis. Multichannel digital temperature indicator is used to measure the temperature. For every 15 min interval, temperature measurement is carried out using K type thermocouple with an accuracy of ± 1 °C for a temperature range of 27 °C–400 °C for a constant voltage supply. This procedure was repeated for each voltage level from 25 to 230 V with an equal interval of 25 V. The surface temperatures of the different specimens are measured at different heat dissipation levels. Thermal conductivity values are obtained using Cartesian coordinate equation and given by  $Q = (kAdT/dx)$ , Where Q is the heat transfer rate and obtained by (VxA), k is the thermal conductivity, A is the cross section area of the specimen, dT is the difference between the surface temperature and dx is the thickness of the specimen. Electrical conductivity measurement is made on the specimens which is connected to (0–30 V) regulated power supply using two 0.5 m single strand wire with a

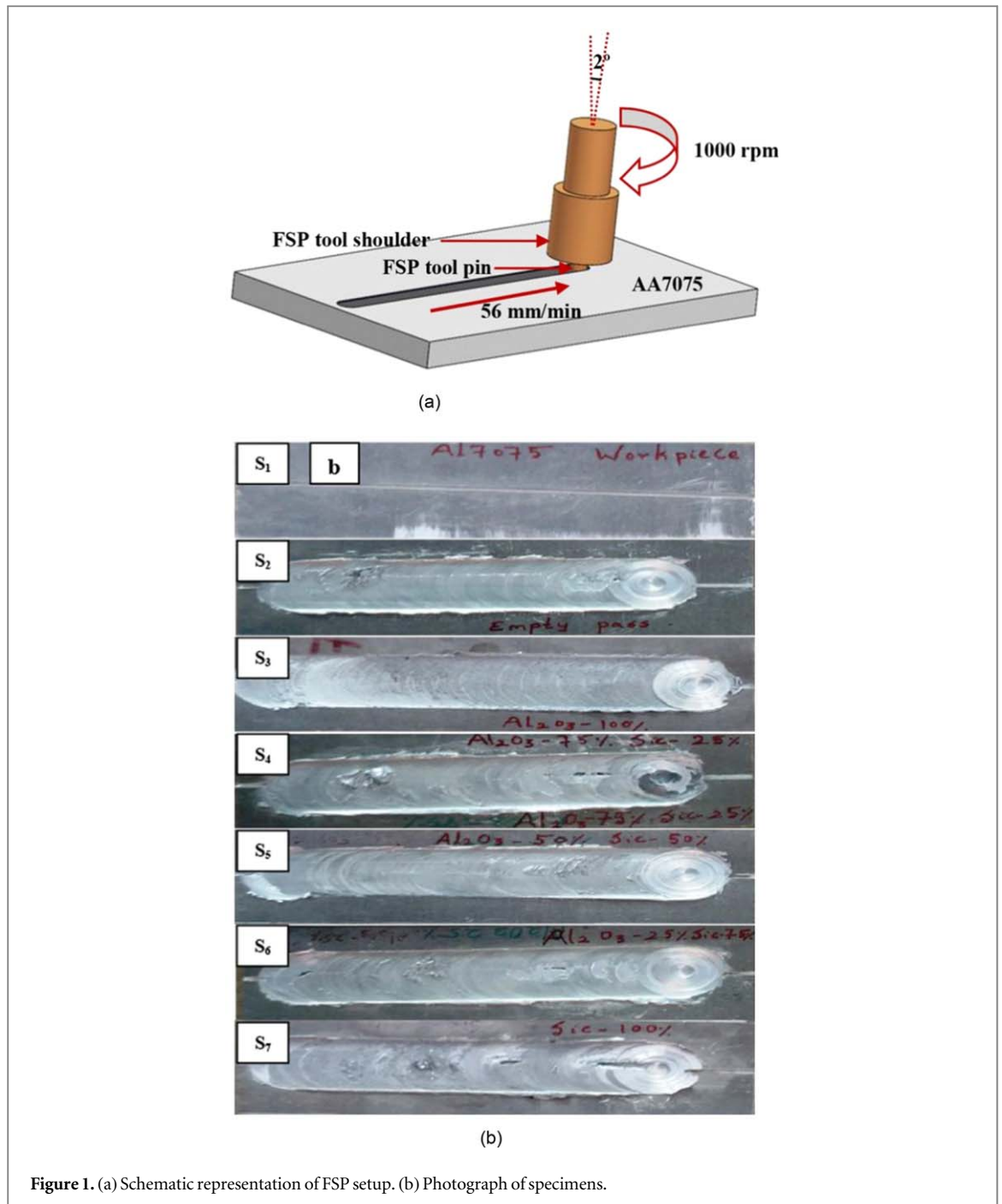


Figure 1. (a) Schematic representation of FSP setup. (b) Photograph of specimens.

resistance of  $3.5\Omega$ . A fixed voltage of 0.2 V is set in regulated power supply and an (0–5 A) ammeter is connected in series with the specimen to measure the current flow in the circuit. Based on current and voltage value, the total resistance of the setup is calculated. Then, the resistance of the specimen is calculated by comparing the known resistance (single strand wire) with the total resistance and %IACS value is obtained. Thermo-mechanical analyzer (TMA Q400) has been used to measure the coefficient of thermal expansion (CTE) for each specimen at a heating rate of  $10\text{ }^{\circ}\text{C min}^{-1}$  under the imposing force of 0.1 N and temperature range of  $30\text{ }^{\circ}\text{C}$ – $400\text{ }^{\circ}\text{C}$ .

### 3. Results and discussion

#### 3.1. Heat generation

FSP is executed on specimens and temperature profiles are obtained during the process over entire length of the specimen using thermal imager and it is shown in figure 4.

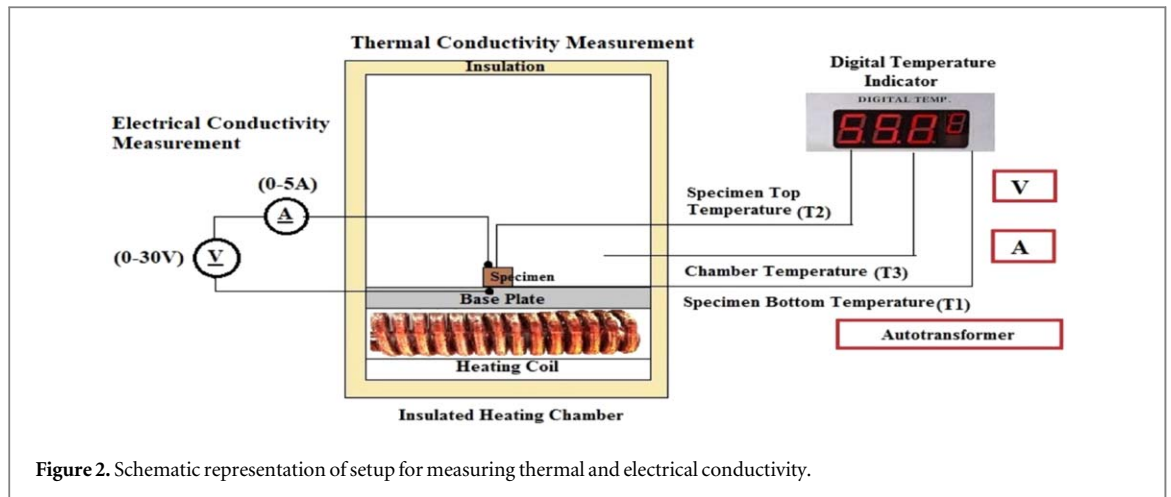


Figure 2. Schematic representation of setup for measuring thermal and electrical conductivity.

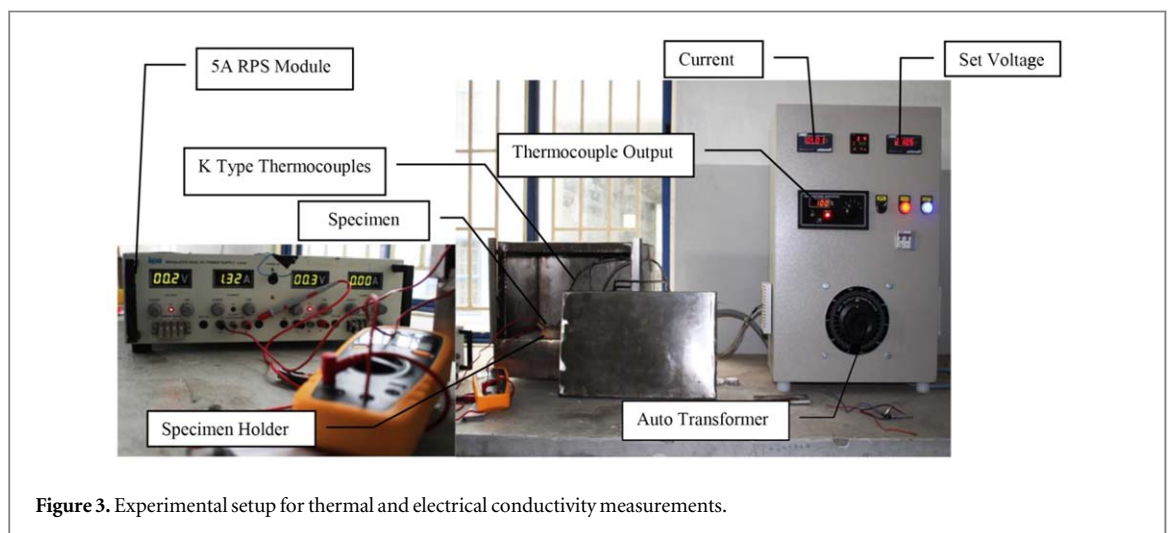


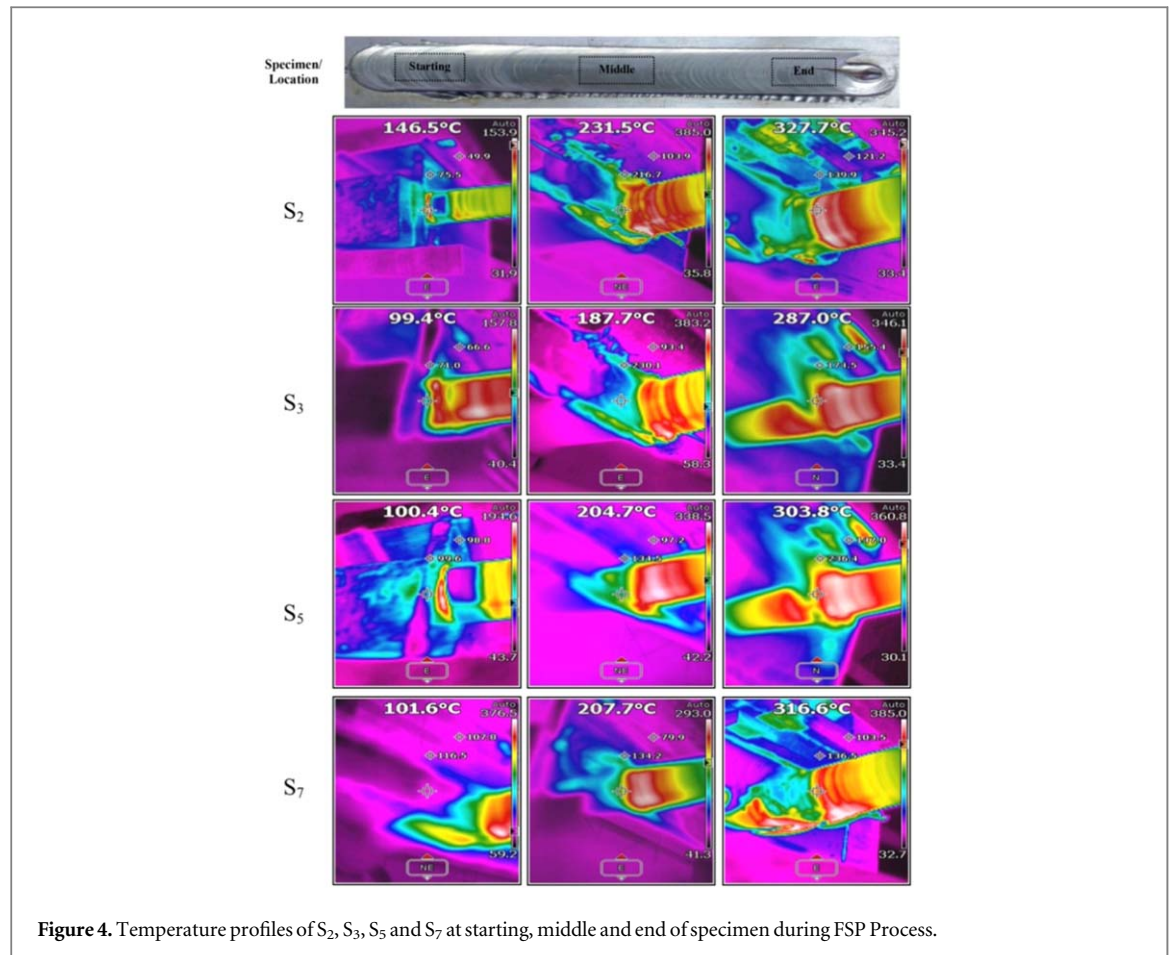
Figure 3. Experimental setup for thermal and electrical conductivity measurements.

Thermal images are captured at different locations of the specimen (Starting, Middle and End points) and indicate that the processing temperature arrived in between 99.4 to 327.7 °C for FSP processed AA7075 composites. This proves that FSP does not melt the base matrix and well mapped with the previous literature [36]. Friction along with plastic deformation causes heat generation and the measurement along the longitudinal section shows in an incremental way due to thermal conductivity behavior of the base material. These images also represent the non-uniformity in temperature distribution around the tool in all the specimens owing to the given 2° tool tilt angle.

With reference to tool movement, higher temperature is obtained in advancing side than the retreating side owing to lower thermal resistance produced by reduced number of grain boundary as seen in optical microstructure of figure 5. Peak temperature about 327.7 °C is measured on the processed specimen without particle reinforcement ( $S_2$ ), which is 51.6% of the melting point (635 °C) of AA7075. During FSP, the potential energy of the electron and phonon has been changed due to the displacement of atoms from their relative position. Increased number of grain boundaries in the FSP region than the base specimen as observed in optical microstructure causes reduction in electron and phononic transportation from FSP depth to the metal surface. This observation is ascribed to lattice dislocations and leads to reduction in temperature than  $S_1$ .

Different thermal characteristics are obtained for the hybrid composites ( $S_3$ – $S_7$ ) because of variation in hardness of the respective materials. Presence of reinforcements is confirmed through optical microstructure and XRD as shown in figures 5 and 6 respectively and XRD represents the reinforcement peaks according to the weight ratios.

Incorporation of ceramic reinforcements retards the grain growth during the metal softening action which reduces the grain size further. The increased number of grain boundaries causes the formation of lattice wave scattering and leads to decrease in temperature compared to  $S_2$ . Addition of alumina particles on AA7075 inflates the formation of Zinc oxide film and predominates the insulating behaviour of the composites than SiC. This formation is authenticated in figure 6. Higher amount of film formation reduces the contact area between tool



and metal surface that leads to reduction in further plastic deformation. It is expected that addition of SiC particles declines the temperature through scattering produced by carbon impurities. In contrary, S<sub>7</sub> (316.6 °C) holds higher peak temperature than S<sub>3</sub> (287 °C) due to higher thermal conductivity nature of SiC particles than Al<sub>2</sub>O<sub>3</sub> [37]. Addition of SiC particles enriches the formation of Mg<sub>2</sub>Si precipitate as shown in figure 6 which is having positive influence on heat generation. With reference to thermal images obtained during experimentation, S<sub>5</sub> endurance the peak temperature of about 303.8 °C and lies comfortably in between the range of S<sub>3</sub> and S<sub>7</sub>. In overall, addition of particle reinforcements reduces the heat generated on the surface. Optimized temperature is necessary to generate plastic deformation and that is achieved through the FSP tool action.

### 3.2. Micro hardness evaluation

Processed part of the specimen of about 15 mm left and right with reference to centre of transverse section has been executed for the Vickers micro hardness indentation and the obtained results are represented in figure 7. FSP specimen without particle reinforcement depicts the superior average hardness values than the base material (175 VHN). Lower micro hardness of base material is caused by coarse grained structure in the as-received condition. The result of higher hardness in S<sub>2</sub> is attributed to the grain refinement structure formed during FSP. Also, the stirring action of pin generates grain size reduction owing to dynamic recrystallization and intensified dislocations in the centre of stir zone that enhances the value of hardness. Decrease in grain size increased the hardness of the composites as per the HallPetch rule and grain morphology is the evident which is obtained through optical microscope images. Increased hardness values are obtained at a distance of 5 mm from the stir zone in the retreating zone compared to advancing zone owing to fine grain formation as seen in figure 5. Scattering of hardness value in the retreating side is more than the advancing side and also in the stir zone.

Incorporation of Al<sub>2</sub>O<sub>3</sub> and SiC reinforcements substantially increases the micro hardness value of the AA7075 composites. This result is attributed by hindering dislocation mechanism, dispersion strengthening and grain boundary strengthening produced by reinforced particles. These mechanisms enhance the strength of the composites. Substantial average hardness value (265 VHN) is designated by S<sub>5</sub> which is superior to all other specimens due to reason of SiC dispersoids pinning with Al<sub>2</sub>O<sub>3</sub> and also by the adhesion of both reinforcements with base matrix AA7075. This observation is clearly revealed in optical microstructure and the presence of both

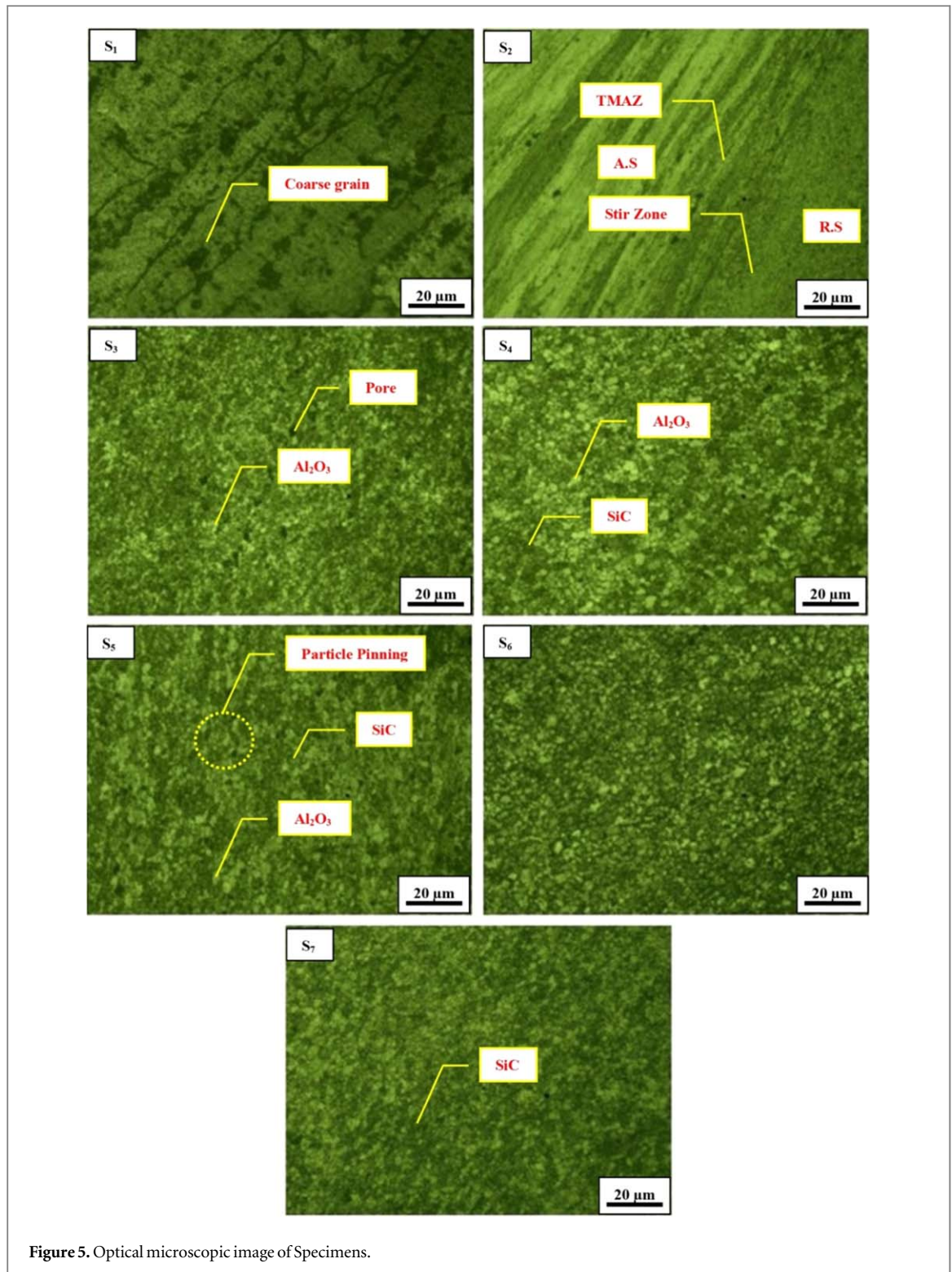


Figure 5. Optical microscopic image of Specimens.

ceramic dispersoids restricts the grain boundary movement. In addition to above, the hardness is also increased due to formation of strengthening intermetallic precipitate  $Al_4C_3$  and the formation is authenticated in figure 6. Addition of SiC particles along with micro structural modification leads to an increase in hardness value when compared to  $Al_2O_3$  as a result of higher hardness and density than  $Al_2O_3$  particle. Increased density reduces the inter-atomic distance of the molecules and this occurrence raises the hardness value. Augmentation of hard SiC particle in the grain boundary region reduces the grain boundary movement which improves the grain refinement and ultimately raises the hardness value. Also, FSP results in significant breakdown of hard SiC particles, that close the pores which enhances the hardness value [38]. Addition of SiC particles generates the local deformation and provides the breaking of grains that modify the hardness value. Addition of  $Al_2O_3$

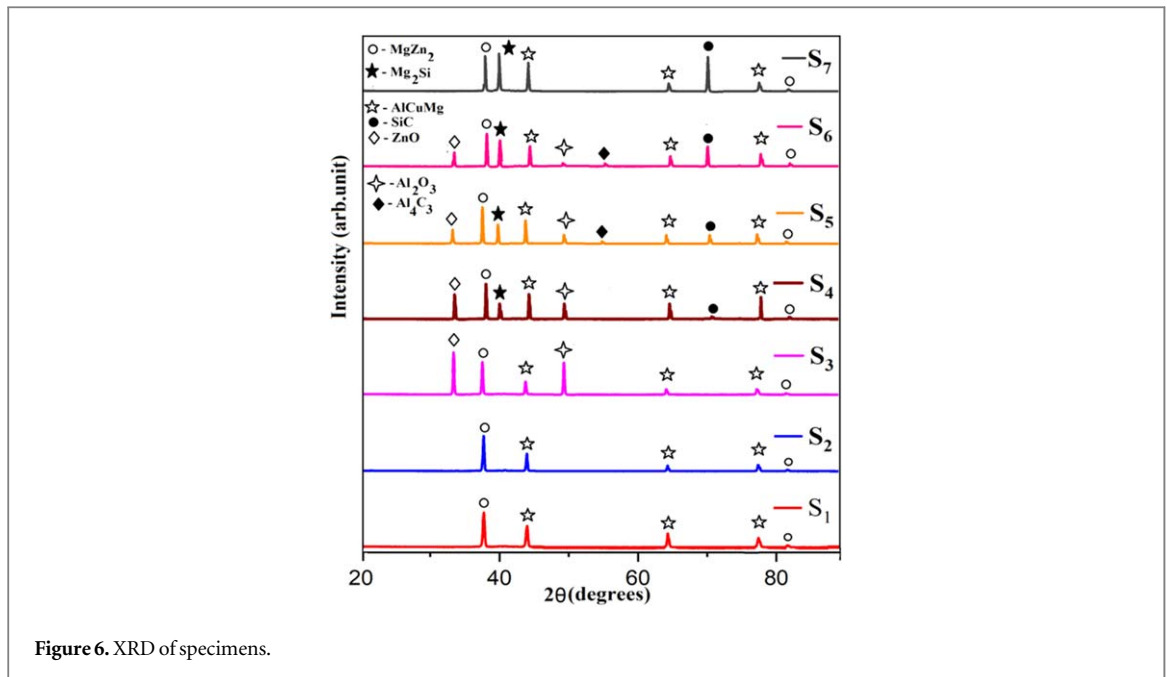


Figure 6. XRD of specimens.

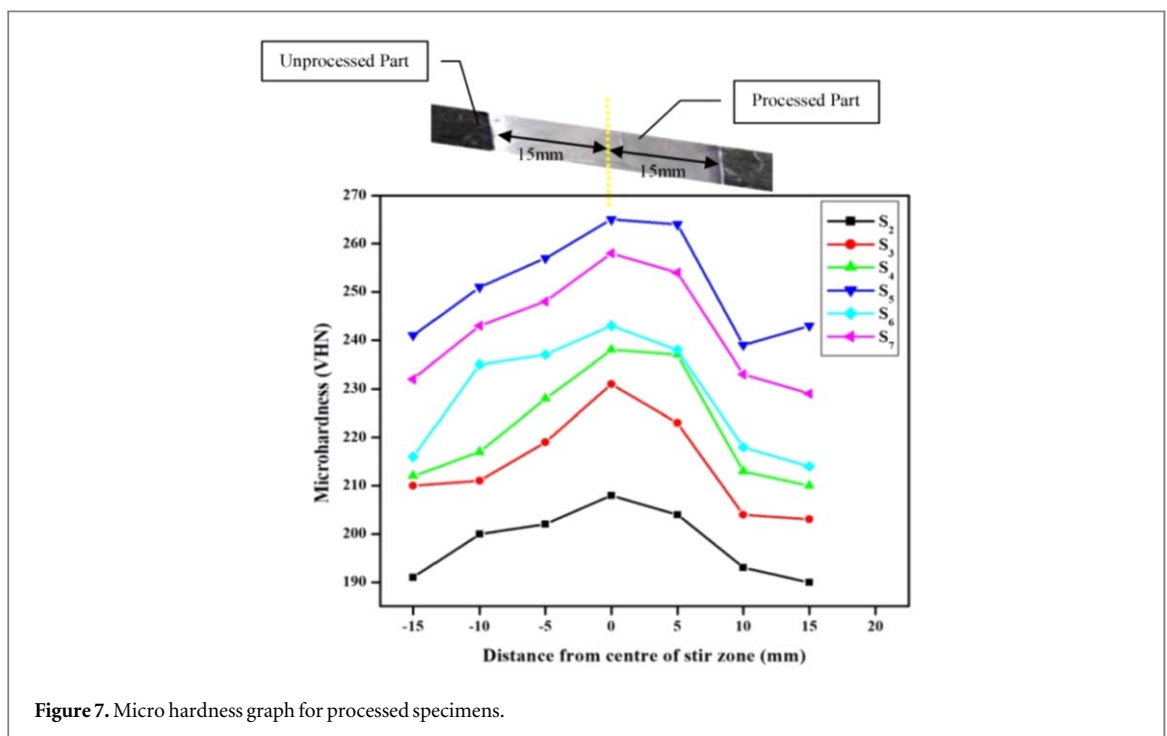


Figure 7. Micro hardness graph for processed specimens.

particles produces agglomerations that induce the pores and increase the inter particle spacing. This phenomenon will decline the hardness value of the composite specimen and is consistent with the results of Tjong *et al* [39]. Presence of large amount of porosity in  $S_3$  surface is revealed in optical and SEM structure than other reinforcement specimens.

### 3.3. Thermal conductivity measurement

Surface temperatures and heat transfer rate are measured using the experimental arrangement and the thermal conductivity values are arrived based on Cartesian coordinate equation. The thermal conductivity observations are noted at distinct levels of temperature from 30 to 400 °C by varying the voltage value through auto-transformer and the results are represented in figure 8. Thermal conductivity is influenced by the excitation of phonons and electrons in the structure of alloys. The change in molecular level is impotent to display the change in thermal conductivity at lowest voltage value of 25 V. Hence the variation in voltage level is maintained in

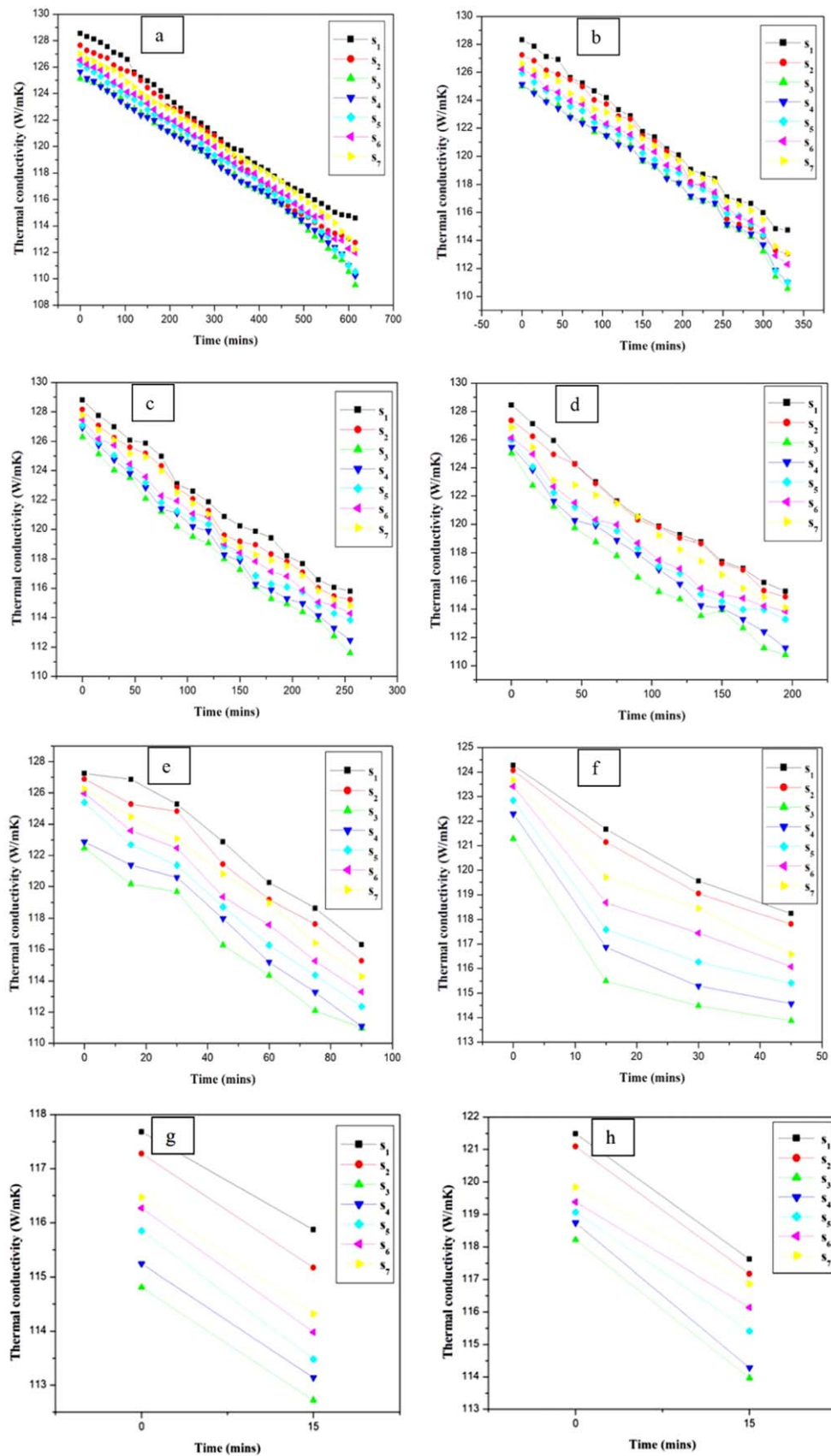
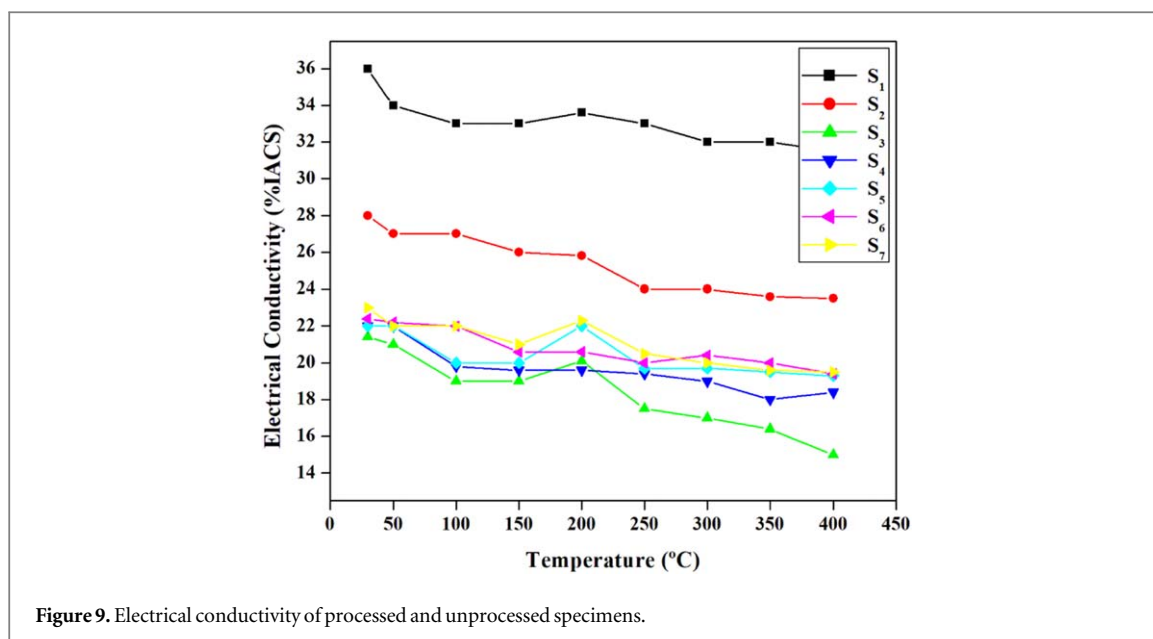


Figure 8. Thermal conductivity of specimens at (a) 50 V (b) 75 V (c) 100 V (d) 125 V (e) 150 V (f) 175 V (g) 200 V (h) 225 V.

between 50 and 225 V. Different voltage input values from 50 V with an interval of 25 V are executed in the experimental analysis to study the variation in thermal conductivity. Surface temperatures of the specimen are measured with the time interval of 15 min for each applied voltage values. During the experimental study, the



heating coil temperature is restricted up to 400 °C because of aforementioned applications. Generally, in solid materials, heat is carried through acoustic phonons and free electrons ( $k = k_p + k_e$ ) where  $k_p$  is the phononic heat conductivity and  $k_e$  is the electronic heat conductivity.  $S_2$  has exhibited lower thermal conductivity value than the base metal ( $S_1$ ) because of intense plastic deformation occurred during FSP process. The grain size of the FSP specimen in the processed area is decreased owing to plastic deformation when compared with the base specimen and this phenomenon is authenticated in figure 5. Increased number of grain boundaries cause scattering of phonons which contributes to the decrease in thermal conductivity. Amplification of grains also provides more adhesion behaviour between the atoms and it amplifies the oxide film formation than the base metal which is witnessed in figures 10(a) and (b) and also in 11(a) and (b). The increased film formation modifies the energy level of electrons and phonons and diminishes the thermal conductivity.

Electron-phonon energy level and relaxation time varied with respect to different input voltages which plays a vital role in the heat transfer process. This effect is clearly revealed in the experimental results. Higher voltage supply ensures less time to reach the maximum temperature of 400 °C. Reinforcement of  $Al_2O_3$  and SiC particles in AA7075 reduce the thermal conductivity value as a result of distinct carrier concentration value between the matrix and surface. Carrier concentration varies with change in hardness value. Particle reinforcement enforces the more quanta of electrons towards scattering effect and transfer lesser amount of electrons which execute the heat transfer phenomena.  $Al_2O_3$  and SiC reinforcement also reduces the kinetic energy of heat carriers as well. Also, phononic interaction with secondary phase particles gets increased and reduces the overall thermal conductivity of the composites.

$S_3$  exhibits the lower thermal conductivity values than other reinforcement specimens owing to higher formation of oxide film confirmed in XRD ( $Al_2O_3$  and ZnO) which acts as thermal boundary resistance. Stronger interface developed in between the AA7075 and  $Al_2O_3$  due to Al-Al matrix results in damping the phononic vibrations. Also, the elastic constant difference between the base matrix and  $Al_2O_3$  causes phonon scattering at the interface paves the way for decreasing the thermal conductivity. This observation is agreed with the results of Geiger *et al* [40]. In overall, addition of  $Al_2O_3$  particles decreases the thermal conductivity of the composites due to the formation of brittle oxide layer that acts as thermal resistance. From the plots, it is identified that increase of temperature lowers the thermal conductivity of AA7075 which support this results already reported by Shivanandha Murthy *et al* [41]. Formation of intermetallic compound ( $Al_4C_3$ ) in  $S_5$  confirmed through XRD and EDX representations in figures 6 and 11(c) respectively provide a thermal barrier for heat transfer and this observation is consistent with the result of Xuan-hui *et al* [42]. Because of intermetallic compound formation,  $S_5$  renders a lower thermal conductivity value of  $117 \text{ W mK}^{-1}$  which is less compared to  $S_7$ . Scattering action of electrons is increased by the pinned effect of reinforced  $Al_2O_3$  and SiC particles and coherence of reinforced  $Al_2O_3$  and SiC with AA7075 base matrix. This observation is also consistent with microscopic images. By incorporating an equal amount of  $Al_2O_3$  and SiC particles in the matrix provides lower porosity defect with higher hardness value and it is presented in figure 10(d). Lower amount of porosity in  $S_5$  accelerates the heat transfer compared to  $S_3$  and higher thermal conductivity value is obtained for specimen  $S_5$ .

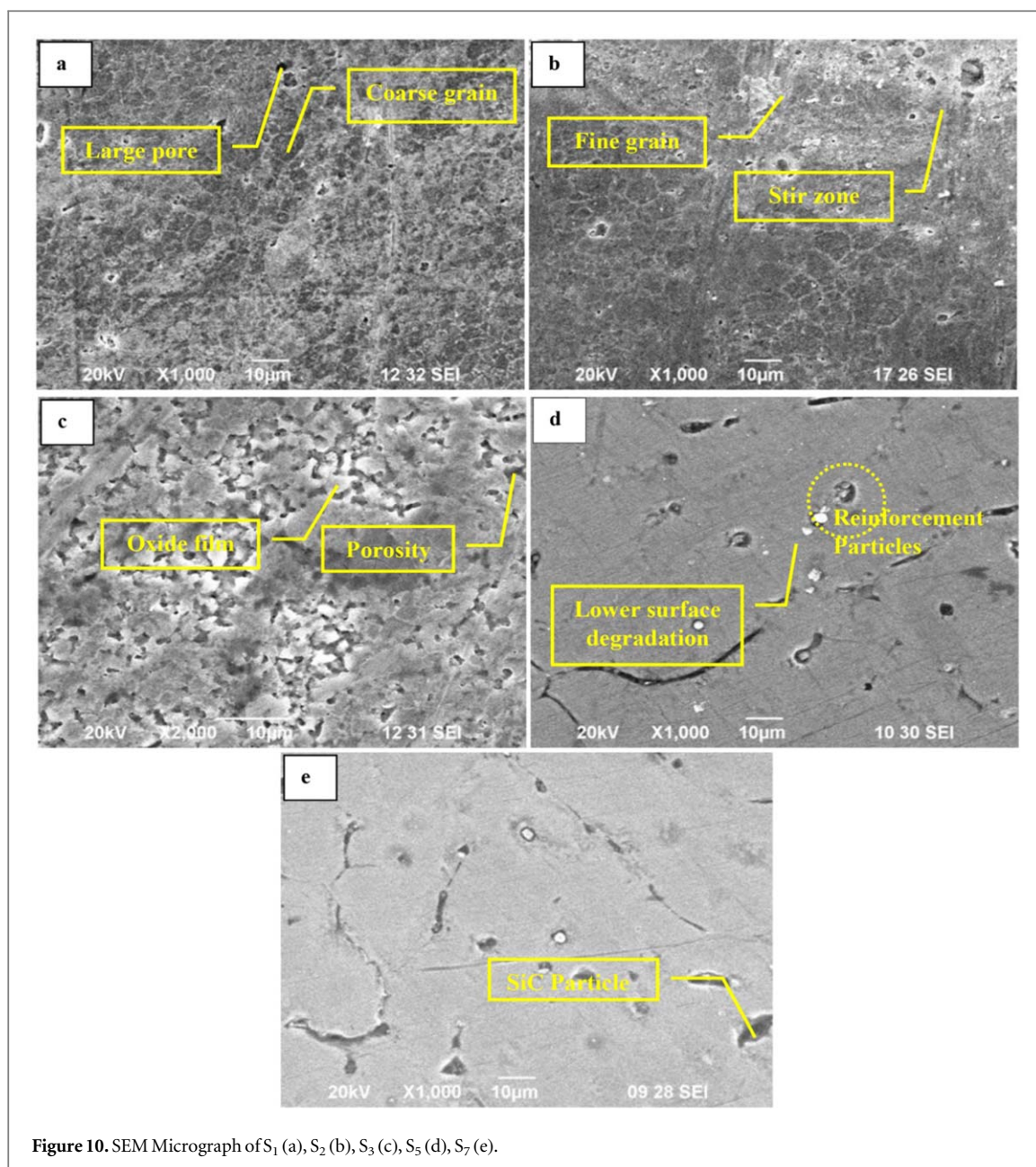


Figure 10. SEM Micrograph of S<sub>1</sub> (a), S<sub>2</sub> (b), S<sub>3</sub> (c), S<sub>5</sub> (d), S<sub>7</sub> (e).

and this observation is revealed in figure 10(c). Being a higher thermal conductivity of SiC particles and Si phononic conductivity nature, S<sub>7</sub> offers more thermal conductivity compared to S<sub>3</sub>. Addition of SiC particles increases the formation of Mg<sub>2</sub>Si precipitates contributes for bridging the heat conduction band which easily transfers the heat. Inflation of carbon particles reduces the mass density of oxide film formed by SiO<sub>2</sub>. This effect reduces the scattering action of phonons and electrons which results in increased thermal conductivity.

### 3.4. Electrical conductivity measurement

As seen in figure 3, when required voltage is applied in the experimental system, the electrons from the Fermi level will gain up the velocity and stimulated to move from the lower band to higher band, which plays a significant role in the electron transport process. The electrical conductivity observations are noted at distinct levels of temperature from 30 to 400 °C using 5 A regulated power supply module, multimeter and by varying the voltage value through auto-transformer and the obtained results are represented in figure 9. Electrical conductivity of S<sub>2</sub>, S<sub>3</sub>, S<sub>4</sub>, S<sub>5</sub>, S<sub>6</sub> and S<sub>7</sub> decreased with respect to increase in temperature. Electrical conductivity of S<sub>2</sub> is 23.21% less than that of S<sub>1</sub> for the applied temperature range because of scattering action and significant change occurs in electron potential and momentum.

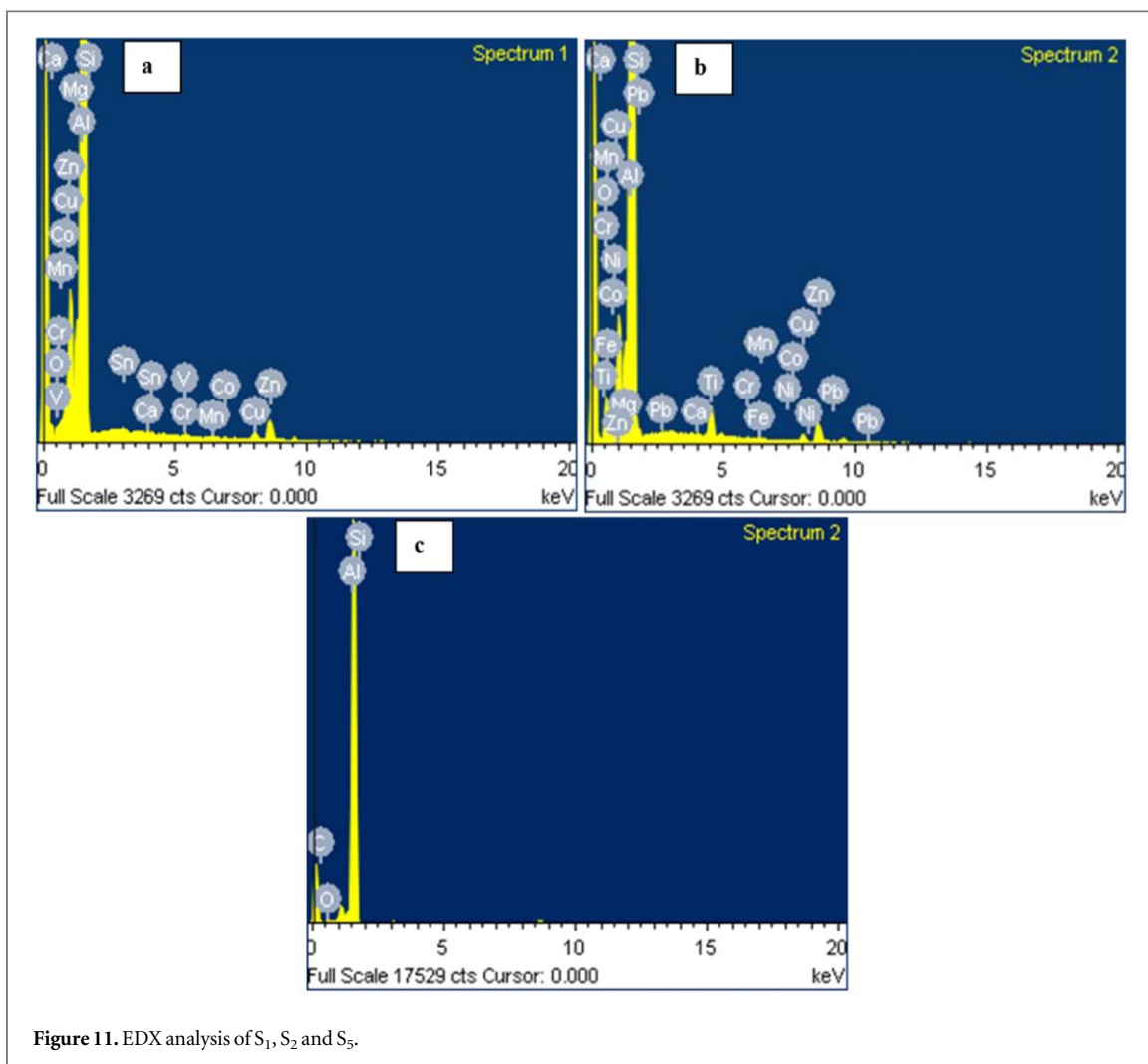
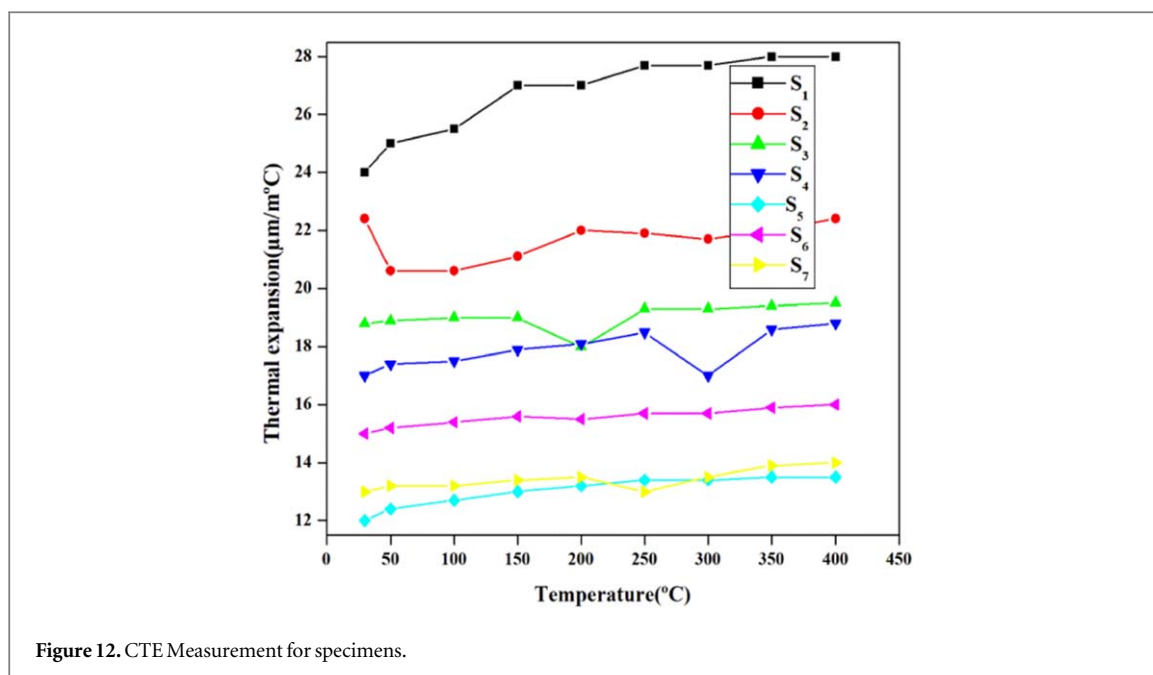


Figure 11. EDX analysis of  $S_1$ ,  $S_2$  and  $S_5$ .

This is attributed to modification in microstructure as well as hardness. Increasing number of grain boundaries as seen in optical microstructure restrict the flow of electrons from bottom end to top surface. Raising temperature in FSP provides the formation of fresh, adherent and stable oxide film over the surface as seen in figure 10(b). This provides a significant scattering action of electrons at larger angles which play a significant role in transportation process. Electrical resistivity of metal composites depends on the amount of alloying elements. Incorporation of  $Al_2O_3$  and SiC secondary phase dispersoids that acts as impurities hinders the electron transport. Formation of impurities reduces the electron potential which favours for reduction in electrical conductivity. Higher amount of  $Al_2O_3$  content in  $S_3$  creates more oxide film formation ( $Al_2O_3$  and ZnO in XRD) and it provides the electrical conductivity of about 12.4% less than that of  $S_7$ .

$Al_2O_3$  dispersoids acts as an electrical insulator and also the electrical resistance of the composites is enhanced by the crystallinity nature of oxide film. Induced porosity as seen in optical microscopic image raises the electrical resistivity of  $S_3$  hybrid composites [43].  $S_5$  having an electrical conductivity of 20.5% IACS which is 3% less than that of  $S_7$  as a result of increased hardness value by  $Al_4C_3$  intermetallics. The enhanced adhesion in between the reinforcement and matrix is also responsible for the increase in hardness value and it is shown in optical microstructure and also in figure 10(d). These results are having good agreement with the experimental analysis of Lee *et al* [44]. Compared to  $S_7$ ,  $S_5$  having a lower surface degradation due to limited porosity and the SEM image of  $S_7$  is shown in figure 10(e). Addition of  $Al_2O_3$  on SiC prevented the electron tunnelling effect that enlarges the electrical resistivity. Decrease of  $Al_2O_3$  and increase of SiC particles improves the electrical conductivity by virtue of discontinuation in the oxide film through SiC particles. According to percolation theory, increase of SiC particles form the conductive path through mutual interconnected SiC particles that raise the electrical conductivity. Being ceramic nature of SiC and presence of carbon impurities in  $S_7$ , the lower electrical conductivity values are obtained for  $S_7$  compared to  $S_2$ . Scattering process is empowered by the carbon impurities which are present in the grain boundary.



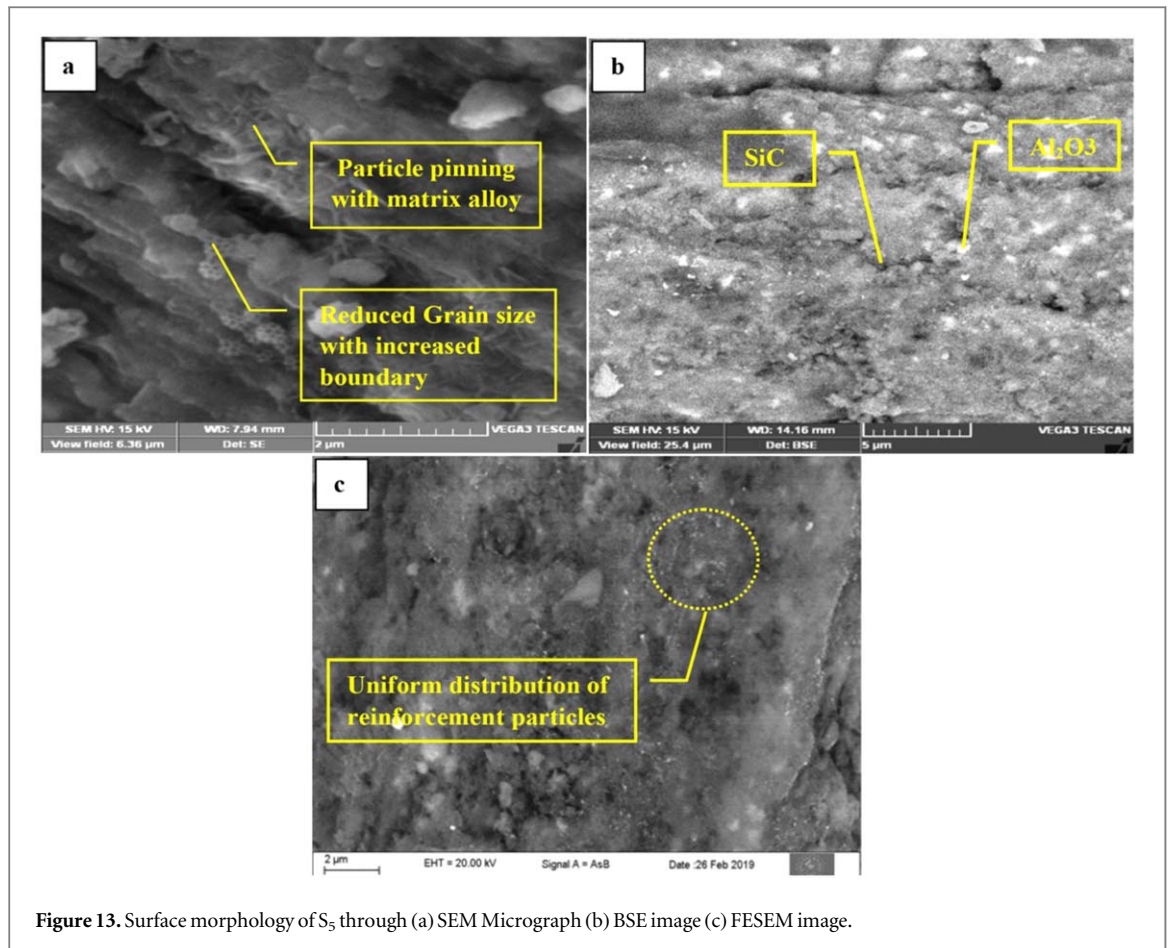
### 3.5. CTE measurement

Figure 12 shows the CTE values of the unprocessed and processed specimens for a wide temperature range of 30 to 400 °C. An agglomeration in specimen S<sub>1</sub> observed in optical structure which is shown in figure 5 induces the residual stress and resulted in higher expansion of the matrix. In FSP processed specimens with and without reinforcement, the values of CTE got decreased through raised hardness. Normally, Aluminium alloy is restricted for particular application in aircraft field owing to its high expansion behaviour. Incorporation of ceramic reinforcements reduces the expansion behaviour of AA7075. In all possibilities, SHC's indicates the lower CTE value compared to both S<sub>1</sub> and S<sub>2</sub> as expected. With reference to lower CTE values, average CTE values of about 21.63  $\mu\text{m m}^{-1} \text{ }^\circ\text{C}$  and 13  $\mu\text{m m}^{-1} \text{ }^\circ\text{C}$  are obtained for S<sub>2</sub> and S<sub>5</sub> respectively. According to the base metal nature, the CTE values of S<sub>2</sub> and S<sub>5</sub> are reduced about 19% and 51% respectively. Presence of strengthening Al<sub>4</sub>C<sub>3</sub> precipitate in S<sub>5</sub> is responsible for lowered CTE values. The stronger interface formed between the reinforcements and base matrix is also responsible for this result. This result declares that hybridization of AA7075 with equal weight ratios of SiC and Al<sub>2</sub>O<sub>3</sub> provides better dimensional stability.

Formation of pores around the oxide film clusters leads to increase the CTE values during the addition of Al<sub>2</sub>O<sub>3</sub> particles in the specimen and it is presented in figure 10(c). This result is matched with the observations made by Geiger *et al* [45]. Comparing to SiC, Al<sub>2</sub>O<sub>3</sub> hold lower hardness and bulk modulus nature. This behavior is also responsible for higher CTE values for Al<sub>2</sub>O<sub>3</sub> reinforced specimens. Addition of SiC reinforcements increases the formation of Mg<sub>2</sub>Si precipitates (observed in XRD), provides a positive influence on CTE values. Hard SiC reinforcements confine the expansion of Al<sub>2</sub>O<sub>3</sub> as well Al matrix. For entire temperature range, CTE values of all the specimens are succeeding in an incremental mode, while temperature increases. Stress matching between the reinforcements and also in between reinforced particles and matrix plays a vital role in CTE analysis. The flow path of the CTE values gets disturbed at some locations as a result of stress mismatch that happens in the specimen. Also, it may be due to increase in vibration amplitude of the adding constituent particles at elevated temperatures.

Investigation results show that S<sub>3</sub> possesses lower hardness, thermal and electrical conductivity values. Higher micro hardness with lower thermal and electrical conductivity values are the requirement of the above said application. Among all specimens, S<sub>5</sub> fulfil the requirements and validated through the following favourable statements.

- Enhanced pinning effect is obtained and depicted in figure 13(a).
- Presence of both reinforcements is confirmed through BSE image and is represented in figure 13(b).
- Uniform particle distribution of Al<sub>2</sub>O<sub>3</sub> and SiC is seen in FESEM image and it is represented in figure 13(c). Incorporation of both reinforcements reduces the grain growth owing to the presence of both Al<sub>2</sub>O<sub>3</sub> and SiC particles along the matrix grain boundary.



**Figure 13.** Surface morphology of S<sub>5</sub> through (a) SEM Micrograph (b) BSE image (c) FESEM image.

The above performance measures can be enhanced by multi pass FSP with hard particle reinforcements like B<sub>4</sub>C, TiC, TaC in future. This may refine the grain structure further which modifies both thermal along with electrical behavior of the composites for aircraft fuselage applications.

#### 4. Conclusion

FSP refined the grain structure of AA7075 and the effective oxide film formation is also ensured when compared with that of the base metal. Uniform dispersion of reinforcement particles in the base matrix is also an evident through the optical microstructure. Temperature measurement provides evidence that FSP process does not melt the base alloy. Thermal resistance is amplified by the addition of Al<sub>2</sub>O<sub>3</sub> particle in the specimens and offers lower thermal conductivity value effectively. Stronger interface developed in between the AA7075 and Al<sub>2</sub>O<sub>3</sub> dispersoids damp the phononic vibrations. This result have attributed also by the formation of brittle oxide film layer of Al<sub>2</sub>O<sub>3</sub> on the base specimen surface. Addition of SiC particles form the conductive path through mutual interconnected SiC particles that raise the thermal and electrical conductivity nature. In all cases, incorporation of ceramic particles reduces the expansion behaviour of AA7075 and it posses better dimensional stability. SEM image symbolize the reduction of discontinuities in the oxide film when the Al<sub>2</sub>O<sub>3</sub> particles increased. Incorporation of SiC particles minimizes the formation of pores on the surface. Significant outcomes of S<sub>5</sub> like higher hardness, lower CTE, lower thermal and electrical conductivity are witnessed by FSP. These observations make the composites to be successfully opted for aircraft applications.

#### Acknowledgments

Authors render the acknowledgement to CSIR-CECRI Karaikudi to complete the Micrographic analysis of the specimens.

## ORCID iDs

K Suganeswaran  <https://orcid.org/0000-0002-9517-0103>

## References

- [1] Mishra R S et al 2003 Friction stir processing: a novel technique for fabrication of surface composite *Materials Science and Engineering: A* **341** 307–10
- [2] Bozkurt Y et al 2011 Microstructure and mechanical properties of friction stir welded particulate reinforced AA2124/SiC/25p-T4 composite *J. Compos. Mater.* **45** 2237–45
- [3] Vatankeh Barenji R et al 2016 Wear properties of Al–Al<sub>2</sub>O<sub>3</sub>/TiB<sub>2</sub> surface hybrid composite layer prepared by friction stir process *J. Compos. Mater.* **50** 1457–66
- [4] Kumar H et al 2018 Microstructure, mechanical and electrical characterization of zirconia reinforced copper based surface composite by friction stir processing *Mater. Res. Express* **5** 086505
- [5] Sharma A et al 2018 Friction stir processing of Al6061–SiC–graphite hybrid surface composites *Mater. Manuf. Processes* **33** 795–804
- [6] Srivastava M et al 2018 Influence of multiple-passes on microstructure and mechanical properties of Al–Mg/SiC surface composites fabricated via underwater friction stir processing *Mater. Res. Express* **5** 066511
- [7] Kumar A et al 2017 Simultaneous improvement of mechanical strength, ductility and corrosion resistance of stir cast Al7075–2% SiC micro- and nanocomposites by friction stir processing *J. Manuf. Processes* **30** 1–13
- [8] Kurt A et al 2011 Surface modification of aluminium by friction stir processing *J. Mater. Process. Technol.* **211** 313–7
- [9] Darras B and Kishta E 2013 Submerged friction stir processing of AZ31 magnesium alloy *Mater. Des.* **47** 133–7
- [10] Weglowski M S and Pietras A 2011 Friction stir processing–analysis of the process *Arch. Metall. Mater.* **56** 779–88
- [11] Badheka V 2016 An experimental investigation of temperature distribution and joint properties of Al 7075 T651 friction stir welded aluminium alloys *Procedia Technology* **23** 543–50
- [12] Patel V V et al 2017 Influence of pin profile on the tool plunge stage in friction stir processing of Al–Zn–Mg–Cu alloy *Trans. Indian Inst. Met.* **70** 1151–8
- [13] Willott W 1967 The Wiedemann–Franz ratio and anomalous lattice conductivity of pure aluminium *Philos. Mag.* **16** 691–702
- [14] Lee S et al 2017 Anomalously low electronic thermal conductivity in metallic vanadium dioxide *Science* **355** 371–4
- [15] Mosso N et al 2017 Heat transport through atomic contacts *Nat. Nanotechnol.* **12** 430
- [16] Tritt T M 2005 *Thermal Conductivity: Theory, Properties, and Applications* (New York: Kluwer Academic / Plenum Publishers)
- [17] Curran J and Clyne T 2005 Thermo-physical properties of plasma electrolytic oxide coatings on aluminium *Surf. Coat. Technol.* **199** 168–76
- [18] Živcová Z et al 2009 Thermal conductivity of porous alumina ceramics prepared using starch as a pore-forming agent *J. Eur. Ceram. Soc.* **29** 347–53
- [19] Klemens P and Williams R 1986 Thermal conductivity of metals and alloys *Int. Met. Rev.* **31** 197–215
- [20] Olafsson P et al 1997 Comparison of experimental, calculated and observed values for electrical and thermal conductivity of aluminium alloys *J. Mater. Sci.* **32** 4383–90
- [21] Salazar-Guapuriche M A et al 2006 Correlation of Strength with Hardness and Electrical Conductivity for Aluminium Alloy 7010 *Mater. Sci. Forum* **519–521** 853–8 Trans Tech Publ
- [22] Santos T et al 2011 Microstructural mapping of friction stir welded AA 7075–T6 and AlMgSc alloys using electrical conductivity *Sci. Technol. Weld. Joining* **16** 630–5
- [23] Jiles D C 2017 *Introduction to the Electronic Properties of Materials* (United Kingdom: Chapman & Hall)
- [24] Mulazimoglu M et al 1989 Electrical conductivity of aluminium-rich Al–Si–Mg alloys *J. Mater. Sci. Lett.* **8** 297–300
- [25] Brandt R and Neuer. G 2007 Electrical resistivity and thermal conductivity of pure aluminum and aluminum alloys up to and above the melting temperature *Int. J. Thermophys.* **28** 1429–46
- [26] Sathiskumar R et al 2013 Characterization of boron carbide particulate reinforced *in situ* copper surface composites synthesized using friction stir processing *Mater. Charact.* **84** 16–27
- [27] Sudhakar I et al 2015 Enhancement of wear and ballistic resistance of armour grade AA7075 aluminium alloy using friction stir processing *Defence Technology* **11** 10–7
- [28] Afromowitz M A 1973 Thermal conductivity of Ga<sub>1–x</sub>Al<sub>x</sub>As alloys *J. Appl. Phys.* **44** 1292–4
- [29] Li B et al 2019 Electrodeposition and properties of Ni–B/SiC nanocomposite coatings *Surf. Eng.* **35** 109–19
- [30] Karthikeyan B et al 2010 A calorimetric study of 7075 Al/SiCp composites *Mater. Des.* **31** S92–5
- [31] Li C et al 2016 Interfacial characteristic and thermal conductivity of Al/diamond composites produced by gas pressure infiltration in a nitrogen atmosphere *Mater. Des.* **92** 643–8
- [32] Murthy H A et al 2013 Effect of TiN particulate reinforcement on corrosive behaviour of aluminium 6061 composites in chloride medium *Bull. Mater. Sci.* **36** 1057–66
- [33] Cho H J et al 2018 Thermal conductivity of copper–diamond composite materials produced by electrodeposition and the effect of TiC coatings on diamond particles *Composites Part B: Engineering* **155** 197–203
- [34] Schindler S et al 2017 Numerical homogenization of elastic and thermal material properties for metal matrix composites (MMC) *Continuum Mech. Thermodyn.* **29** 51–75
- [35] Essawy H and El-Nashar D 2004 The use of montmorillonite as a reinforcing and compatibilizing filler for NBR/SBR rubber blend *Polym. Test.* **23** 803–7
- [36] Mishra R S and Ma. Friction Z 2005 stir welding and processing *Materials Science and Engineering: R: Reports* **50** 1–78
- [37] Senthilvelan T et al 2013 Fabrication and Characterization of SiC, Al<sub>2</sub>O<sub>3</sub> and B<sub>4</sub>C Reinforced Al–Zn–Mg–Cu Alloy (AA 7075) Metal Matrix Composites: A Study *Advanced Materials Research* **622–623** 1295–9 Trans Tech Publ
- [38] Ma Z et al 2006 Microstructural modification of as-cast Al–Si–Mg alloy by friction stir processing *Metallurgical and Materials Transactions A* **37** 3323–36
- [39] Tjong S C 2007 Novel nanoparticle-reinforced metal matrix composites with enhanced mechanical properties *Adv. Eng. Mater.* **9** 639–52
- [40] Geiger A et al 1997 Electrical and thermal conductivity of discontinuously reinforced aluminum composites at sub-ambient temperatures *Acta Mater.* **45** 3911–4

- [41] Murthy K S *et al* 2017 Mechanical and thermal properties of AA7075/TiO<sub>2</sub>/Fly ash hybrid composites obtained by hot forging *Progress in Natural Science: Materials International* **27** 474–81
- [42] Qu X-H *et al* 2011 Review of metal matrix composites with high thermal conductivity for thermal management applications *Progress in Natural Science: Materials International* **21** 189–97
- [43] Kim K J *et al* 2013 Control of electrical resistivity in silicon carbide ceramics sintered with aluminum nitride and yttria *J. Am. Ceram. Soc.* **96** 3463–9
- [44] Lee E *et al* 2007 The effect of thermal exposure on the electrical conductivity and static mechanical behavior of several age hardenable aluminum alloys *Eng. Fail. Anal.* **14** 1538–49
- [45] Geiger A *et al* 1993 Effect of reinforcement particle size on the thermal conductivity of a particulate silicon carbide-reinforced aluminium-matrix composite *J. Mater. Sci. Lett.* **12** 420–3